Response of a swirl flame to inertial waves

Alp Albayrak, Deniz A Bezgin and Wolfgang Polifke

Abstract
Acoustic waves passing through a swirler generate inertial waves in rotating flow. In the present study, the response of a premixed flame to an inertial wave is scrutinized, with emphasis on the fundamental fluid-dynamic and flame-kinematic interaction mechanism. The analysis relies on linearized reactive flow equations, with a two-part solution strategy implemented in a finite element framework: Firstly, the steady state, low-Mach number, Navier–Stokes equations with Arrhenius type one-step reaction mechanism are solved by Newton's method. The flame impulse response is then computed by transient solution of the analytically linearized reactive flow equations in the time domain, with mean flow quantities provided by the steady-state solution. The corresponding flame transfer function is retrieved by fitting a finite impulse response model. This approach is validated against experiments for a perfectly premixed, lean, methane-air Bunsen flame, and then applied to a laminar swirling flame. This academic case serves to investigate in a generic manner the impact of an inertial wave on the flame response. The structure of the inertial wave is characterized by modal decomposition. It is shown that axial and radial velocity fluctuations related to the eigenmodes of the inertial wave dominate the flame front modulations. The dispersive nature of the eigenmodes plays an important role in the flame response.

1. Introduction

Thermo-acoustic combustion instabilities have been a subject of intensive studies, with important applications in power and propulsion systems. One important aspect is the flame transfer function (FTF), which describes the response of the flame heat release rate to flow perturbations. In the literature, a wide variety of studies can be found, ranging from low order models[1–3] to high fidelity numerical simulations,[4,5] with the objective to determine the FTF and to understand the underlying physics.

For premixed swirling flames, the flame dynamics comprises several acoustic-flow-flame interaction mechanisms, see e.g. the overview given in Section 5 of the lecture notes by Polifke.[6] *Rotational waves* – also known as *inertial waves*[7] in fluid dynamics – generated by acoustic waves propagating across the swirl generator have received increased attention in recent years.[8–13]

The overall flame dynamics results from superposition of the various interaction mechanisms. Straub and Richards[8] demonstrated the importance of this superposition by changing the axial position of the swirler within a fuel nozzle, which resulted in a significant alteration of the combustor stability. The corresponding sensitivity of the FTF to swirler position was confirmed experimentally and numerically by Komarek and Polifke[10] and explained in terms of the different time scales of acoustic and inertial waves. Simple models for the response functions of the respective contributions to the overall FTF were formulated in terms of distributed delays, but the fluid-dynamic mechanism by which inertial waves modulate the heat release rate of the flame was not analyzed.

Hirsch et al.[9] modeled the overall FTF of a swirl flame by considering the transport equation for

Faculty of Mechanical Engineering, Technical University of Munich, Munich, Germany

Corresponding author:
Alp Albayrak, Thermo-Fluid Dynamics Group, Technical University of Munich, Boltzmannstr. 15, Garching D-85748, Germany.
Email: albayrak@tfd.mw.tum.de

perturbations of azimuthal vorticity. Effective *secondary* velocity fluctuations, which result from vorticity fluctuations, were then computed with the Biot–Savart law. Palies et al.[11,12] modeled inertial waves as convective tangential velocity perturbations, adopting actuator disk theory proposed by Cumpsty et al.[14] and Cumpsty and Marble.[15] The corresponding flame response was modeled by the level set method. It was argued that the tangential velocity perturbations change the turbulent burning speed, thus causing heat release rate fluctuations. Acharya and Lieuwen[13] observed in numerical simulations that tangential velocity perturbations generate axial as well as radial flow fluctuations, which contribute to the flame response.

The objective of the present study is to gain further insight into the fluid mechanics of swirl flame response to flow perturbations. An academic configuration, i.e. a laminar swirling flame is investigated. Linearized reactive flow (LRF) equations are formulated and solved to compute the respective impulse responses (IRs) to perturbations of axial and tangential velocity. Axisymmetric inertial waves with three-dimensional modal structure[16,17] are observed to have a significant impact on the flame shape and overall surface area.

In the first part of this paper, we propose a method for accurate and fast estimation of FTFs based on LRF equations. Linearized Navier–Stokes equations are commonly used for stability analysis of non-reactive flows. Recently, Qadri[18] extended this approach for reactive flows by including the linearized species transport equation with Arrhenius type one-step chemistry. A slightly different approach was proposed by Blanchard et al.[19] to estimate the flame response by direct numerical linearization over a steady state solution of a reactive flow simulation. Qualitative agreement with experiments was achieved. In both studies, steady state solutions were achieved via transient simulation combined with selective frequency damping.

In the present work, Newton's method is employed to obtain the steady state solution. Instead of relying on direct numerical linearization, the governing equations are linearized analytically. Transient simulations are performed to obtain the IRs. The corresponding FTFs are retrieved by fitting a discrete finite IR model to the time series data. Results are quantitatively validated against the experiment from Kornilov et al.[5] for a laminar Bunsen flame.

In the second part, the LRF-based method for computation of FTFs is applied to a swirling laminar flame. IRs for both flame response contributions are computed, the interaction between inertial waves and the flame front kinematics is explicated with the help of snapshots of the flow fields. Following Albayrak and Polifke,[17] a modal decomposition is applied and the perturbation structures are characterized as dispersive

waves with non-zero components in axial, radial and azimuthal coordinate directions. Their distinct Bessel function type eigenmodes are shown to be important for the flame response. In particular, the structure of the inertial wave eigenmodes implies that a tangential velocity perturbation induces axial as well as radial velocity perturbations, which modulate the flame front and thus generate heat release rate perturbations.

2. LRF model for the flame response

This section presents the approach for FTF computations based on LRF equations. The set of governing equations for a low Mach number flow reads as

$$\nabla \cdot \boldsymbol{u} = \frac{1}{\rho c_p T}[\nabla \cdot (\lambda \nabla T) + \dot{\omega}_T] \tag{1a}$$

$$\frac{D\boldsymbol{u}}{Dt} = -\frac{1}{\rho}\nabla p + \frac{1}{\rho}\nabla \cdot (\mu \nabla \boldsymbol{u}) \tag{1b}$$

$$\frac{DY_F}{Dt} = \frac{1}{\rho c_p}[\nabla \cdot (\lambda \nabla Y_F) + \dot{\omega}_F] \tag{1c}$$

$$\frac{DT}{Dt} = \frac{1}{\rho c_p}[\nabla \cdot (\lambda \nabla T) + \dot{\omega}_T] \tag{1d}$$

$$p_0 = \rho RT \tag{1e}$$

where $\boldsymbol{u}$ is flow velocity vector, ρ is density, c_p is heat capacity at constant pressure, λ is the thermal conductivity, μ is the dynamic viscosity, T is temperature, $\dot{\omega}_T$ is the heat release rate, $\dot{\omega}_F$ is the reaction rate, Y_F is the mass fraction of fuel, R is the specific gas constant, p_0 is the thermodynamic pressure, p is hydrodynamic pressure.

The above set of equations was derived for binary air-fuel mixture under the following assumptions: In lean hydrocarbon/air flames, the properties of air dominate the mixture and the heat capacity of the mixture is close to that of air. Furthermore, the value of heat capacity is changing only slightly over a wide temperature range. Therefore, heat capacity of air and fuel is assumed to be equal and independent of temperature. In hydrocarbon/air flames, Lewis number changes only slightly across the flame front. In many theoretical approaches, the Lewis number of all species is set to unity, see Poinsot and Veynante.[20] Accordingly, we assume the Lewis number of fuel to be unity. Majda and Lamb[21] proposed a low Mach number assumption for combustion at low Mach numbers and strong heat release. The low Mach number assumption splits the pressure into a thermodynamic and a hydrodynamic pressure component.[22] Following Williams[23] and Poinsot and Veynante,[20] the reaction rate term $\dot{\omega}_F$ for

a premixed flame is modeled by an irreversible one-step Arrhenius law

$$\dot{\omega}_F = -A\rho Y_F \exp^{-\beta/\alpha} \exp\left(-\frac{\beta(1-C)}{1-\alpha(1-C)}\right) \quad (2)$$

where $C = (T - T_1)/(T_2 - T_1)$ is the normalized temperature and α, β and the preexponential factor A are model parameters. Further explanation of the model parameters is given in the Appendix. The heat release rate $\dot{\omega}_T = -\Delta h_{f,F}^0 \dot{\omega}_F$ is calculated with the mass enthalpy of formation of fuel $\Delta h_{f,F}^0$. Sutherland's viscosity model is made use of

$$\mu = \frac{A_s T^{3/2}}{T + S} \quad (3)$$

The temperature dependence of the thermal conductivity λ is modeled as

$$\lambda = \lambda_1 \frac{T}{T_1} \quad (4)$$

where λ_1 is the thermal conductivity of the fluid at inflow temperature T_1, see Williams.[23]

The steady state solution of equation (1) is computed using Newton's method. Using these base solutions, the linearized equations (see equation (15) in Appendix) are solved in time domain. The goal is to compute the linear flame dynamics, in particular the flame IR.

The sets of equations (1) and (15) were implemented in the finite element method framework Freefem++.[24] P2-P1 Taylor-Hood elements are used, i.e. velocity, temperature and mass fraction are discretized by second order polynomials, while first-order polynomials are used for pressure. Solution algorithms for the steady state case and the linearized unsteady dynamics are described in the next subsections.

The numerical methods were validated against CFD simulations (OpenFOAM) and experiments on a Bunsen flame by Kornilov et al.[5] and Duchaine et al.[25] results are presented below. Further information on the FreeFem++ model constants, OpenFOAM simulations and the experimental setup can be found in the Appendix.

2.1. Steady state computations

The governing equations are nonlinear due to the convective terms and the combustion model. Newton's method finds a solution for a nonlinear system of equations of type $F(x) = 0$ by an iterative process, which starts from an initial guess x_0

$$x_{n+1} = x_n - (J_F(x_n))^{-1} F(x_n) \quad n = 0, 1, 2, \ldots, \quad (5)$$

where $x = [u, T, Y_F, p]$ denotes the field variables and J_F stands for the Jacobian matrix of $F(x)$.

Newton's method converges if the initial guess is sufficiently close to the solution, i.e. within the convergence radius of the problem. To provide such an initial guess, we employ the low Reynolds and low Peclet number limit ($Re, Pe \to 0$) of the governing equations. In this limit, the Navier–Stokes equations reduce to Stokes equations, while the energy and species transport equations reduce to pure diffusion equations. The use of Stokes equation as an initial guess for solving the Navier–Stokes equations NSE via Newtons method is well documented in the literature, see Kim et al.[26] Furthermore, the convergence radius is enlarged by artificially increasing the values of viscosity μ and thermal conductivity λ by a factor of ten. Once the convergence is achieved, the diffusive coefficients are decreased by 5% and Newton's method is re-started. This loop is carried on until the correct values of viscosity and thermal conductivity are retrieved.

Convergence of Newton's method is checked by evaluating the error

$$err = \sum \frac{|\delta x|_\infty}{|x|_\infty} \quad (6)$$

where $|\cdot|_\infty$ is the L-infinity norm and δ is the increment between two consecutive iteration steps in Newton's method. The diffusive coefficients are reduced, whenever $err < 0.1$. Iterations cease once the viscous terms μ, λ attain their physical values and the error $err < 10^{-5}$.

The resulting mean flow fields and flame shapes compare well against OpenFOAM results, see Figures 1 and 2, which show the spatial distributions of axial velocity and heat release rate, respectively. Both figures show normalized quantities, i.e. $u_z/\max(u_z)$ and $\dot{\omega}_T/\max(\dot{\omega}_T)$, thus the colormap ranges from 0 to 1. Simulations with fixed wall temperature – see the right plot – show a slight deviation in flame shape, because combustion parameters of the one-step chemistry model were fitted to the adiabatic case, while OpenFOAM uses a two-step chemistry model from the literature.[27] Further information on the OpenFOAM simulation setup is given in the Appendix.

2.2. Linearized dynamics computations

A linearization of equation (1) is described in the Appendix. As in the steady case, P2-P1 Taylor-Hood elements are employed for the spatial discretization of these equations. Implicit Backwards Euler scheme is used to advance in time. The convective terms are discretized with Characteristic Galerkin method.[28]
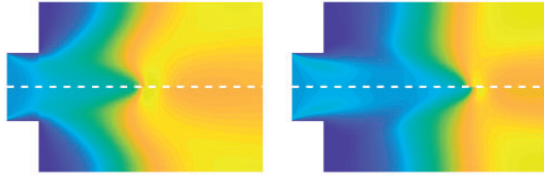
Figure 1. Comparison of the normalized axial velocity field. Left: Adiabatic. Right: Fixed temperature walls. Upper half: OpenFOAM. Lower half: FreeFEM++.
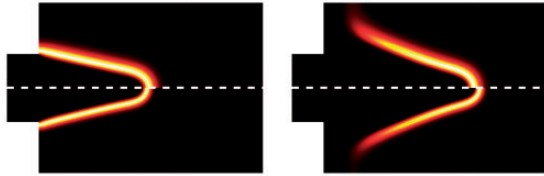

Figure 2. Comparison of the normalized heat release rate. Left: Adiabatic. Right: Fixed temperature walls. Upper half: OpenFOAM. Lower half: FreeFEM++.

Figure 3. IR of the laminar flame with adiabatic (left) and isothermal (right) walls. The adiabatic flame OpenFOAM (- - -) and FreeFEM++ (——).

Figure 4. FTF of Kornilov flame. Left: Adiabatic. Right: Fixed wall temperature. OpenFOAM (- - -), FreeFEM++ (——) and experiments [5] (○).

In the LRF framework, there exists no noise contribution as the initial state is stationary. Therefore, the flame response is simply obtained by an impulsive perturbation in inlet flow velocity $u_z' = \bar{u}_z \varepsilon \delta(t)$. It is important to note that this perturbation is equivalent to an acoustic wave in a compressible framework. The Dirac impulse is approximated by a normal distribution, i.e.

$$\delta(t) \approx \frac{1}{a\sqrt{\pi}} \exp^{-(t/a)^2} \qquad (7)$$

where a is the standard deviation and should be close to zero to approximate the Dirac function accurately. However, very small values are not feasible numerically. In this work, the value of $a = 0.1\,\text{ms}$ is chosen such that $a < \tau_{IR}/20$, where τ_{IR} indicates the IR length. This is appropriate for the frequency range of 0–1000 Hz.

By definition, the flame IR $h(t)$ is the normalized heat release rate fluctuations caused by the impulsive velocity perturbation and reads as

$$h(t) \equiv \frac{\dot{Q}'(t)}{\bar{\dot{Q}}\varepsilon} \qquad (8)$$

where $\dot{Q} = \int \dot{\omega}_T \mathrm{d}V$ is the global heat release rate. The IR contains the same information as FTF. It is also possible to retrieve the corresponding FTF by fitting a discrete-time finite IR model to the IR.

Figures 3 and 4 prove that the FreeFEM++ simulation of the linearized dynamics achieves good quantitative agreement for both IR and FTF. For the
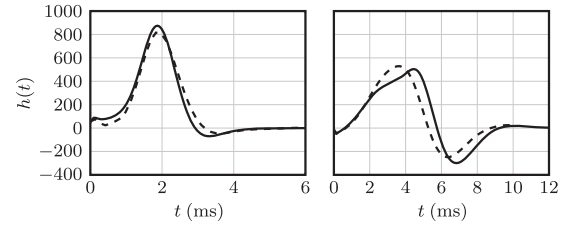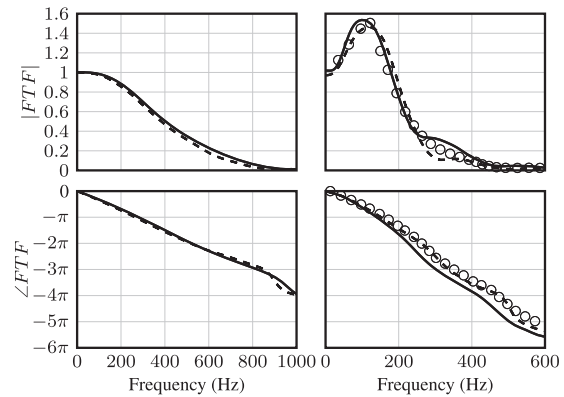
isothermal walls, the FTF results match well with the experiments[5] and also the OpenFOAM simulations. For the cases with adiabatic walls, good agreement is also met. Here, the comparison is only shown against the OpenFOAM simulations, as there are no experimental data available.

3. Case study: A swirling flame

After validation of the proposed numerical method with the example of slit flames, we proceed to a laminar swirling V-flame stabilized on a bluff body, see Figure 5. A 2D domain with cylindrical symmetry is considered, with inner and outer radii of the annular duct $r_i = 1\,\text{mm}$ and $r_o = 2\,\text{mm}$, respectively. The duct length between the swirler – which is not included in the computational domain, but assumed to be located just upstream of the inlet boundary – and the combustion chamber is 5 mm.

Following Kerrebrock,[16] the flow profile at the inlet is approximated by an uniform axial velocity and a solid body rotation, i.e.

$$\bar{\boldsymbol{u}} = [\bar{u}_z, 0, Kr] \qquad (9)$$

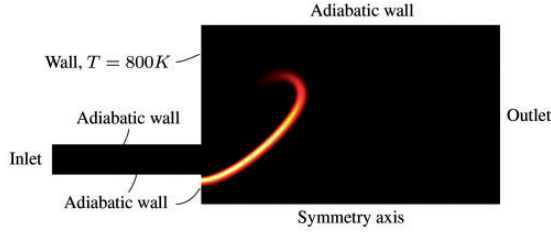where $K = 1000\,\text{s}^{-1}$ is the circulation and $\bar{u}_z = 2\,\text{m/s}$.

Figure 5. Normalized heat release rate of swirling V-flame.

Figure 6. Major contributions to the response of a swirl flame to an acoustic perturbation, c.f. Figure 9 in Komarek and Polifke.[10]

First the steady mean fields are computed. Figure 5 shows the steady state heat release rate field. In order to anchor a V-flame, the upper side wall and the combustion chamber wall are cooled to 800 K. Subsequently, LRF equations are solved to compute the IR caused by velocity perturbations upstream of the swirler. Since the swirler is excluded, the perturbation structure at the swirler exit should be modeled. This is done by the actuator disk theory following Palies et al.,[11,12] which introduces two different velocity perturbations. One of them is the upstream *axial* velocity perturbation itself, which is conserved throughout the swirler due to continuity. The corresponding flame response mechanism is illustrated in the upper branch of Figure 6 denoted by F_A. The other perturbation occurs in the tangential velocity due to Kutta condition and should be identified as the source of an *inertial wave*.[7] As will be shown below, axial as well as radial velocity perturbations result, which have distinct mode structures. The first block F_{MC} in the lower branch of Figure 6 stands for the mode conversion from acoustic axial velocity to inertial wave. The second block F_S stands for the corresponding *swirl* component of the flame response.

Since the present approach is linear, the velocity perturbations can be applied separately. Similar to the Bunsen flame calculations in the previous section, we first compute the IRs. To account for the first contribution, an axial velocity perturbation at the inlet is introduced as

$$u'_z(z = 0, t) = \bar{u}_z \varepsilon \delta(t) \qquad (10)$$

For the inertial wave contribution, the Kutta condition is applied, i.e. the tangential velocity perturbation is defined as $u'_\theta = u'_z \tan \alpha$, where α indicates the swirl angle. By applying modal decomposition on the linearized Navier–Stokes equations, Albayrak and Polifke[17] showed that any tangential velocity perturbation can be constructed by modes. $M_j(m_k r)$ is the *j*-th eigenmode and given by

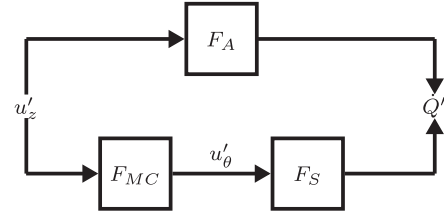$$M_j(xr) = J_j(xr) - \frac{J_1(xr_o)}{Y_1(xr_o)} Y_j(xr) \qquad (11)$$

where J_j and Y_j are the first and second kind of Bessel function, respectively. These eigenmodes are found analytically by deriving the dispersion relation and applying the impermeability condition as $u'_r = 0$ at annular duct walls. For simplicity, the perturbation is approximated by the first eigenmode

$$u'_\theta(z = 0, t) \approx \bar{u}_z \tan(\alpha) \varepsilon \chi_1 M_1(m_1 r) \delta(t) \qquad (12)$$

where m_k is the *k*-th positive root of $M_1(xr_i) = 0$ for *x*. The prefactor χ of the eigenmodes is calculated through

$$\chi_k = \frac{\int_{r_i}^{r_o} r M_1(m_k r) \mathrm{d}r}{\int_{r_i}^{r_o} r M_1(m_k r)^2 \mathrm{d}r} \qquad (13)$$

Two separate simulations are performed with the above boundary conditions, i.e. equations (10) and (12). Again, the Dirac delta function is approximated by a normal distribution function with small standard deviation. The corresponding heat release rate fluctuations describe the IRs denoted by h_A and h_S, which are plotted in Figure 7(c). In the following subsection, the IR results are interpreted.

3.1. Interpretation of the response to inertial waves

Since the configuration is 2D axisymmetric, a tangential velocity perturbation by itself does not generate any heat release rate fluctuations. The swirl contribution to the flame response is generated through the axial and radial velocity perturbations that result from inertial waves. As explicated in a previous study,[17] the modal decomposition applied on a swirling flow generates also perturbations of axial and radial velocity. Since we approximated the tangential velocity perturbation at the swirler exit only with the first eigenmode (see equation (12)), the corresponding eigenmodes for axial and radial velocity perturbations read

$$\hat{u}_r \propto M_1(m_{1,1} r) \qquad (14\mathrm{a})$$

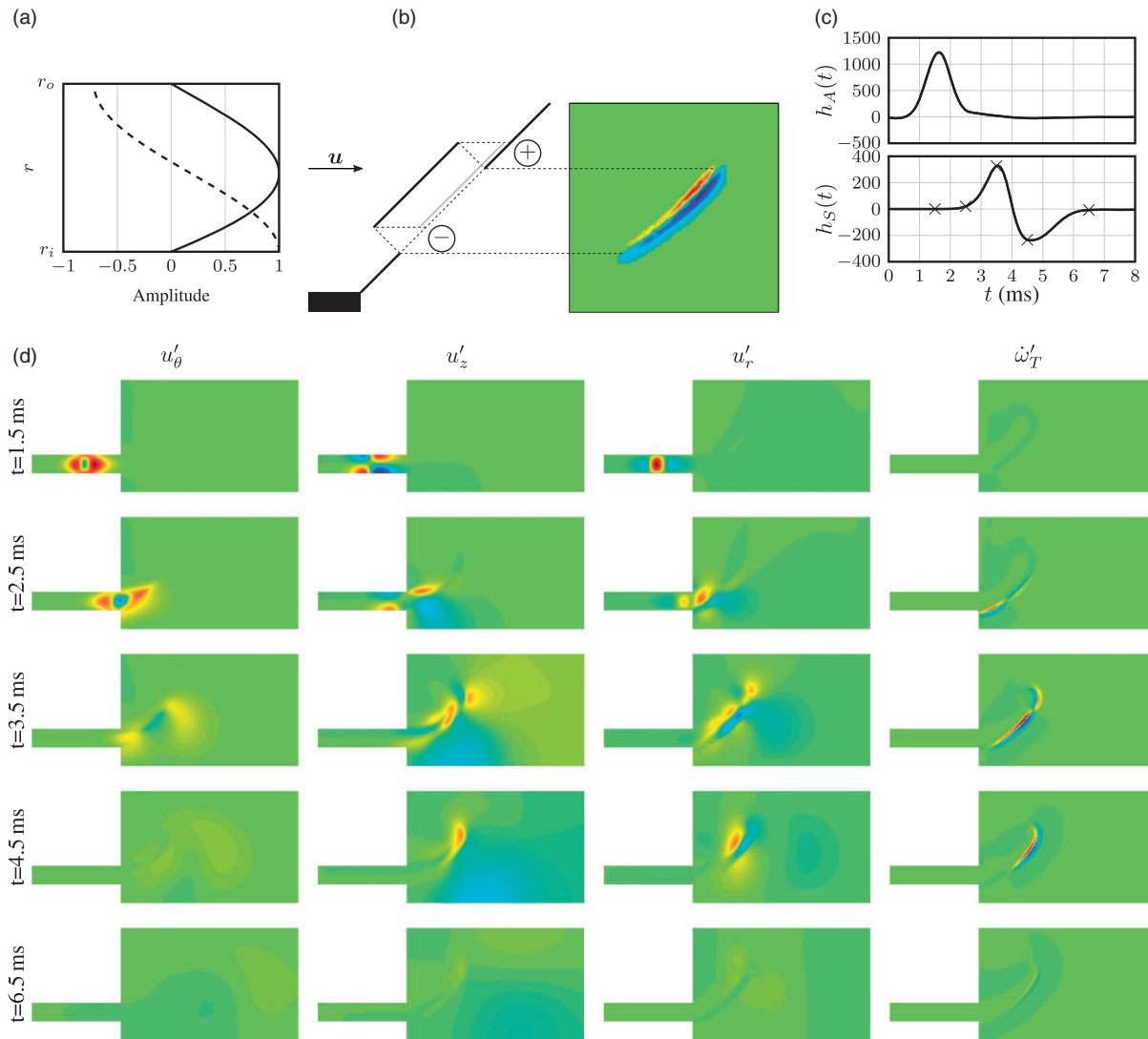$$\hat{u}_z \propto M_0(m_{1,1} r) \qquad (14\mathrm{b})$$

Figure 7. Response of flame front to an inertial wave generated by a perturbation of tangential velocity at the inlet. (a) Normalized eigenmode of $\hat{u}_z$ (- - -); $\hat{u}_\theta$ and $\hat{u}_r$ (——). (b) Sketch of a flame perturbed by negative axial velocity. Left: Level-set framework. Right: $\dot{\omega}'_T$ in LRF framework. (c) Flame impulse responses to axial (top) and tangential (bottom) perturbation. Crosses indicate times of snapshots shown in Figure 7(d). (d) Snapshots of normalized tangential, axial, radial velocities and heat release rate (from left to right) after an impulsive perturbation of tangential velocity.

The eigenfunction profiles are plotted against the duct radius in Figure 7(a). The amplitudes in *x*-axis are normalized with the maximum values. These profiles are also observed in the snapshots in Figure 7(d), which depict the results of the IR simulation with tangential velocity perturbation as defined in equation (12). All quantities in the snapshots are normalized with maximum values. Thus, the range of the color-maps is from −1 (blue) to 1 (red).

The tangential and radial velocities (shown in the first and third columns, respectively) exhibit the pattern of the $M_1(m_{1,1}r)$ eigenmode. In the third column, the axial velocity perturbations are shown, which have a

$M_0(m_{1,1}r)$ eigenmode pattern. All velocity perturbations exhibit dispersive behavior in the axial direction during the propagation in the duct (see Albayrak and Polifke[17]), which is clearly seen in the first row. For example, in axial velocity perturbation, a pocket of a wave travels in front and followed by another wave pocket with a negative sign.

In the last column of Figure 7(d), the linearized heat release rates are presented. We interpret the source terms by the level-set approach proposed by Blumenthal et al.[2] The correspondence between the LRF framework and the level-set approach is demonstrated in Figure 7(b). A snapshot of a flame

is illustrated, which is perturbed by a negative axial velocity perturbation. In the level-set framework (left plot), the flame is moved towards upstream due to the kinematic balance between the flow velocity and the flame speed. The perturbed flame surface generates a deficit and an overlap in flame surface area as indicated in the figure with − and + signs, respectively. The change in the flame surface area can be easily visualized by projecting the perturbed flame to the unperturbed flame. As discussed by Blumenthal et al.,[2] the unsteady heat release rate is generated by the flame surface area fluctuations. In the linearized heat release rate $\dot{\omega}_T$ framework (right plot), the movement of the flame surface can be understood as a positive $\dot{\omega}'_T$ in the upstream region and a negative $\dot{\omega}'_T$ in the downstream region.

The shape of the IR caused by a tangential velocity perturbation (see Figure 7(c)) is explained using the snapshots in Figure 7(d). The first row in the snapshots corresponds to the simulation time of 1.5 ms. At this time, no heat release rate fluctuation is generated (see lower part in Figure 7(c)) as the inertial waves still propagates through the duct and did not reach the flame yet. The negative axial velocity region around the inner duct wall arrives first at the flame base and displaces the flame in the upstream direction. In level-set framework, this is characterized by a leading overlap (denoted by a plus sign in Figure 7(b)) and a following gap (denoted by a minus sign in Figure 7(b)) in flame surface area. It is important to note that when assessing the net influence of a pocket, the leading part has a stronger weight due to a larger radius compared to the following part. Therefore, the IR starts with a positive contribution. At a slightly later time, the positive axial velocity perturbation around the outer duct wall arrives to the flame and displaces the flame towards downstream, which causes a negative contribution. Both, the impact of the negative (inner wall) and positive (outer wall) axial velocity perturbations can be observed in the $\dot{\omega}'_T$ plot at 2.5 ms with a sign change in the middle of the flame. Combination of these both effects yields a weakly positive slope of the IR at early times. The downstream displaced flame reaches the flame tip and the corresponding flame surface area gap leaves the domain, i.e. the maximum IR is observed at 3.5 ms. After this point, the flame response starts to sink. This trends continues till the upstream displaced flame, caused by the negative velocity perturbation at the inner wall, reaches the flame tip at 4.5 ms. The only remaining gap is then convected through the flame surface till the initial flame is recovered around 6.5 ms. This is also called as the restoration mechanism by Blumenthal et al.[2]

Although the configuration is simplified, we argue that it is an ideal case to study the flame-flow interaction mechanisms without complication. This strong argument can be supported by the following observations: (1) By definition, the FTF is a global quantity as the heat release rate is integrated over the whole flame surface. Therefore, impact of turbulence related flame wrinkles on the FTF is negated. (2) In swirling flows, there exist unstable coherent structures, i.e. precessing vortex cores that are particularly important for the burner stability (see Oberleithner et al.[29]). However, the energy content of these structures clustered at a distinct high frequency, which is not explicitly related to the inertial waves generated at the swirler.

The IRs in Figure 7(c) show qualitative similarities with results of Komarek and Polifke[10] for a turbulent swirling flame, i.e. the axial velocity contribution shows a Gaussian-like positive IR and the inertial wave contribution has a positive response followed by a negative. The integral of the axial velocity contribution gives one, whereas the inertial wave contribution gives zero. These values are also in agreement with the low frequency limit of the FTF described by Polifke and Lawn.[30] Two distinct time lags are observed. The axial perturbation contribution has zero time lag (in low Mach number framework, the speed of sound is infinity). The swirl contribution has a convective time lag (≈ 2 ms), which is related to the distance from the swirler to the flame. This also confirms the actuator disk model by Palies et al.[11,12] Our approach further suggests that the tangential velocity perturbations generate axial and radial perturbations, which disturb the flame front and cause heat release rate fluctuations. This is not predicted by the actuator disk model, where the turbulent flame speed modulations caused by the tangential velocity perturbations are the major cause of the flame response. Moreover, the inertial wave structures brings a physical explanation to the work from Acharya and Lieuwen,[13] where the generation of axial and radial velocity perturbations is observed in numerical simulations.

4. Conclusion

An idealized swirling flame is investigated with emphasis on the mechanism of flame response to tangential velocity perturbations. We identify these perturbations as inertial waves, which are accurately described by linear theory. A method based on LRF equations is thus developed to identify the flame IR. The linear framework is ideal to scrutinize the interaction between inertial waves and a swirl flame. Linearized low Mach number Navier–Stokes equations with reduced order one-step chemistry are implemented in a finite element method framework in order to describe flame dynamics. The solution algorithm consists of two parts: First, Newton's method is employed to find the steady state

solution. Then, the LRF equations are solved with an impulsive flow perturbation to obtain the flame IR. This approach is thoroughly validated for a laminar Bunsen flame.

The approach is then applied to a swirling flame. By analyzing the snapshots of the perturbed LRF fields, characteristics of the response of the flame to a tangential velocity perturbation are elucidated. Inertial waves comprise perturbations in all three velocity components; fluctuations of heat release rate are explained in terms of the kinematic balance of flame front propagation with the axial and radial velocity components.

The results bring new insight to the dynamics of swirling flames and can be used to explain some previous results. Acharya and Lieuwen[13] observed in numerical simulations that the acoustic waves crossing the swirler generate hydrodynamic waves, which generate unsteady heat release. Similarly, Hirsch et al.[9] attributed the cause of the unsteady heat release to the secondary velocity fluctuations using the azimuthal vorticity equations. We can precisely identify these flow structures as inertial waves, and compute their spatio-temporal evolution. Note that the argument of Palies et al.,[11,12] i.e. that flame response is caused by changes in turbulent flame speed that result from swirl number variations, cannot be applied to the present laminar swirl flame.

A possible extension of this work is to apply the approach to a realistic configuration with turbulence to study 3D structures. Solution of the Reynolds-averaged Navier–Stokes equations (RANS), time averaged reactive flow fields from large eddy simulation (LES) or experiment can be used as the linearization point. The LRF is a powerful tool for fast and accurate IR estimations. Moreover, it can be easily converted to a linear eigenvalue problem, which can be used for the global stability and sensitivity analysis.

Acknowledgements

Declaration of Conflicting Interests

The author(s) declared no potential conflicts of interest with respect to the research, authorship, and/or publication of this article.

Funding

References

1. Schuller T, Durox D and Candel S. A unified model for the prediction of laminar flame transfer functions: comparisons between conical and V-flame dynamics. *Combust Flame* 2003; 134: 21–34.
2. Blumenthal RS, Subramanian P, Sujith R, et al. Novel perspectives on the dynamics of premixed flames. *Combust Flame* 2013; 160: 1215–1224.
3. Cho JH and Lieuwen TC. Laminar premixed flame response to equivalence ratio oscillations. *Combust Flame* 2005; 140: 116–129.
4. Tay-Wo-Chong L, Bomberg S, Ulhaq A, et al. Comparative validation study on identification of premixed flame transfer function. *J Eng Gas Turb Power* 2012; 134: 8.
5. Kornilov VN, Rook R, ten Thije Boonkkamp JHM, et al. Experimental and numerical investigation of the acoustic response of multi-slit Bunsen burners. *Combust Flame* 2009; 156: 1957–1970.
6. Polifke W. Combustion instabilities. In: Anthoine J and Hirschberg A (eds) *Advances in aeroacoustics and applications*. Rhode-St-Genèse: Von Karman Institute, 2004, pp.22–33.
7. Gallaire F and Chomaz JM. Instability mechanisms in swirling flows. *Phys Fluids* 2003; 15: 2622–2639.
8. Straub DL and Richards GA. Effect of axial swirl vane location on combustion dynamics. In: *International gas turbine and aeroengine congress & exhibition*, Indianapolis, Indiana, 7–10 June 1999. New York, NY: ASME.
9. Hirsch C, Fanaca D, Reddy P, et al. Influence of the swirler design on the flame transfer function of premixed flames. In: *ASME turbo expo*, Reno, NV, USA, 6–9 June 2005, pp.151–160. New York, NY: American Society of Mechanical Engineers.
10. Komarek T and Polifke W. Impact of swirl fluctuations on the flame response of a perfectly premixed swirl burner. *J Eng Gas Turb Power* 2010; 132: 7.
11. Palies P, Durox D, Schuller T, et al. The combined dynamics of swirler and turbulent premixed swirling flames. *Combust Flame* 2010; 157: 1698–1717.
12. Palies P, Schuller T, Durox D, et al. Modeling of premixed swirling flames transfer functions. *Proc Combust Inst* 2011; 33: 2967–2974.
13. Acharya V and Lieuwen T. Role of azimuthal flow fluctuations on flow dynamics and global flame response of axisymmetric swirling flames. In: *52nd aerospace sciences meeting*, National Harbor, Maryland, 13–17 January 2014.
14. Cumpsty NA, Nicholas A and Marble FE. The generation of noise by the fluctuations in gas temperature into a turbine. Technical Report CUED/A TURBO/TR57, Cambridge, England, 1974.
15. Cumpsty N and Marble F. The interaction of entropy fluctuations with turbine blade rows; a mechanism of turbojet engine noise. *Proc Royal Soc Lond A* 1977; 357: 323–344.

16. Kerrebrock JL. Small disturbances in turbomachine annuli with swirl. *AIAA J* 1977; 15: 794–803.

17. Albayrak A and Polifke W. Propagation velocity of inertial waves in cylindrical swirling flow. In: *23nd interntional congress on sound and vibration (ICSV23)*, Athens, Greece, 10–14 July 2016. Auburn University, Alabama: IIAV.

18. Qadri UA. *Global stability and control of swirling jets and flames*. PhD Thesis, University of Cambridge, UK, 2014.

19. Blanchard M, Schuller T, Sipp D, et al. Response analysis of a laminar premixed M-flame to flow perturbations using a linearized compressible Navier-Stokes solver. *Phys Fluids* 2015; 27: 043602.

20. Poinsot T and Veynante D. *Theoretical and numerical combustion*. 2nd ed. Philadelphia: Edwards, R. T. Incorporated, 2005. [ISBN 1-930217-10-2].

21. Majda A and Lamb KG. Simplified equations for low Mach number. *Dynam Issues Combust Theor* 2012; 35: 167.

22. McMurtry PA, Jou W-H, Riley J, et al. Direct numerical simulations of a reacting mixing layer with chemical heat release. *AIAA J* 1986; 24: 962–970.

23. Williams FA. *Combustion theory*. 2nd ed. Boston, Massachusetts, US: Addison-Wesley Publishing Company, 1985.

24. Hecht F. New development in freefem++. *J Numer Math* 2012; 20: 251–265.

25. Duchaine F, Boudy F, Durox D, et al. Sensitivity analysis of transfer functions of laminar flames. *Combust Flame* 2011; 158: 2384–2394.

26. Kim SD, Lee YH and Shin BC. Newton's method for the Navier-Stokes equations with finite-element initial guess of stokes equations. *Comput Math Appl* 2006; 51: 805–816.

27. Bibrzycki J, Poinsot T and Zajdel A. Investigation of laminar flame speed of Ch4/N2/O2 and Ch4/Co2/O2 mixtures using reduced chemical kinetic mechanisms. *Arch Combust* 2010; 30: 287–296.

28. Pironneau O. On the transport-diffusion algorithm and its applications to the Navier-Stokes equations. *Numer Math* 1982; 38: 309–332.

29. Oberleithner K, Sieber M, Nayeri CN, et al. Three-dimensional coherent structures in a swirling jet undergoing vortex breakdown: stability analysis and empirical mode construction. *J Fluid Mech* 2011; 679: 383–414.

30. Polifke W and Lawn CJ. On the low-frequency limit of flame transfer functions. *Combust Flame* 2007; 151: 437–451.

31. Weller HG, Tabor G, Jasak H, et al. A tensorial approach to computational continuum mechanics using object-oriented techniques. *Comput Phys* 1998; 12: 620–631.

Appendix

The experimental setup is described in detail by Kornilov et al.[5] A perfectly premixed lean Methane-air flame with equivalence ratio is $\phi = 0.8$ is considered in a multi slit burner. Center to center distance between two slits is 5 mm. Both, the duct radius and the length are both 1 mm. Since the flow is laminar and axisymmetric, only one-half of one slit flame is chosen as the numerical domain. The plenum does not modify the flow profiles in the combustion region and thus is excluded. The flame is stabilized on the wall that is cooled to temperature of $T = 373$ K. The bulk flow velocity in the duct is 1 m/s and the inflow temperature is $T_1 = 293$ K. Thermal conductivity at inflow is $\lambda_1 = 0.0257$ W/(mK).

The CFD simulations are performed in OpenFOAM, which is a finite volume solver.[31] Second-order spatial discretization (Gaussian integration with central differences) and time integration (backward) schemes are employed. The modified version of reactingFOAM is used, i.e. low Mach number assumption and Schmidt number of 0.7. Reduced two step chemistry mechanism 2S-CM2 as described by Bibrzycki et al.[27] is used to model the Methane-air combustion.

The linearized version of equation (1) that is implemented in FreeFem++ reads

$$
\begin{aligned}
(\rho' \bar{T} &+ \bar{\rho} T') \nabla \cdot \boldsymbol{u}' + \bar{\rho} \bar{T} \nabla \cdot \bar{\boldsymbol{u}} \\
&= \frac{1}{c_p} \left[\nabla \cdot \left(\lambda' \nabla \bar{T} + \bar{\lambda} \nabla T' \right) + (\dot{\omega}_T)' \right]
\end{aligned}
\tag{15a}
$$

$$
\begin{aligned}
\bar{\rho} \left(\frac{\overline{\mathrm{D}} \boldsymbol{u}'}{\overline{\mathrm{D}} t} + \boldsymbol{u}' \cdot \nabla \bar{\boldsymbol{u}} \right) &+ \rho' \bar{\boldsymbol{u}} \cdot \nabla \bar{\boldsymbol{u}} \\
&= -\nabla p' + \nabla \cdot (\mu' \nabla \bar{\boldsymbol{u}} + \bar{\mu} \nabla \boldsymbol{u}')
\end{aligned}
\tag{15b}
$$

$$
\begin{aligned}
\bar{\rho} \left(\frac{\overline{\mathrm{D}} Y_F'}{\overline{\mathrm{D}} t} + \boldsymbol{u}' \cdot \nabla \bar{Y}_F \right) &+ \rho' \bar{\boldsymbol{u}} \cdot \nabla \bar{Y}_F \\
&= \frac{1}{c_p} \left[\nabla \cdot \left(\lambda' \nabla \bar{Y}_F + \bar{\lambda} \nabla Y_F' \right) + (\dot{\omega}_F)' \right]
\end{aligned}
\tag{15c}
$$

$$
\begin{aligned}
\bar{\rho} \left(\frac{\overline{\mathrm{D}} T'}{\overline{\mathrm{D}} t} + \boldsymbol{u}' \cdot \nabla \bar{T} \right) &+ \rho' \bar{\boldsymbol{u}} \cdot \nabla \bar{T} \\
&= \frac{1}{c_p} \left[\nabla \cdot \left(\lambda' \nabla \bar{T} + \bar{\lambda} \nabla T' \right) + (\dot{\omega}_T)' \right]
\end{aligned}
\tag{15d}
$$

where $\overline{(.)}$ indicates a mean quantity and $(.)'$ a perturbed quantity. Linearized material derivative is given by

$$
\frac{\overline{\mathrm{D}}(.)}{\overline{\mathrm{D}} t} = \frac{\partial (.)}{\partial t} + \bar{\boldsymbol{u}} \nabla (.)
\tag{16}
$$

For the combustion model, the parameters α, β and A have to be chosen. The model parameter α represents the total heat release of the flame, while β is a non-dimensional formulation of the activation temperature.

α can be calculated by $\alpha = (T_2 - T_1)/T_2$, while β is given as $\beta = \alpha T_a/T_2$ with the activation temperature T_a. Poinsot and Veynante[20] give two typical values for β, $\beta = 8$ for turbulent combustion and $\beta = 18.4$ for premixed hydrocarbon–air flames. We find that the lower beta value of 8 yields thicker flame structures which are closer to the results from OpenFOAM. The preexponential factor is $A = 2.25 \cdot 10^9$. We adjust the preexponential factor such that the flame speed of the reference flame is captured. We use the analytic expression for the flame speed Poinsot and Veynante[20]

$$s_L = \frac{1}{\beta} exp\left(-\frac{\beta}{2\alpha}\right)\left(2A\frac{\lambda_1}{\rho_1 c_p}\right)^{0.5}\left(1 + \frac{1.344 - 3\alpha}{\beta}\right) \quad (17)$$

The constants in Sutherland's viscosity model are $A_s = 1.67212 \cdot 10^{-6}$ kg/(sm$\sqrt{K}$) and $S = 170.672$ K.